Vibronic interaction in CO_3^- photo-detachment: Jahn-Teller effects beyond structural distortion and general formalisms for vibronic Hamiltonians in trigonal symmetries

Issaka Seidu[a]

Department of Chemistry, Carleton University,

Ottawa, Ontario, K1S5B6, Canada and

Department of Chemistry and Biomolecular Sciences,

University of Ottawa, 10 Marie Curie,

Ottawa, Ontario, K1N6N5, Canada

Prateek Goel[a]

Department of Chemistry, University of Florida,

Gainesville, Florida, 32601, United States

Xiao-Gang Wang

Department of Chemistry, Queen's University,

Kingston, Ontario, K7L3N6, Canada

Bo Chen

Department of Chemistry, Pennsylvania State University,

State College, Pennsylvania, 16801, United States

Xue-Bin Wang

Pacific Northwest National Laboratory,

Richland, Washington, 99352, United States

Tao Zeng

Department of Chemistry, Carleton University,

Ottawa, Ontario, K1S5B6, Canada

[a] These two authors made equal contributions.

Abstract

Recently, the negative ion photoelectron spectrum of CO_3^- was reported and the second lowest energy band is assigned to the close-lying $^3E''$ and $^3E'$ states that undergo Jahn-Teller distortions (*Chem. Sci.*, 2016, **7**, 1142). This assignment is based on the Born-Oppenheimer approximation and the assumption of a static Jahn-Teller effect that distorts the CO_3 structure from D_{3h} to C_{2v} symmetry. In this work, we employ a 4 states 6 modes vibronic coupling model to investigate the triplet band and uncover the dynamic and non-adiabatic nature of the Jahn-Teller and pseudo-Jahn-Teller interactions in the triplet states. The apparent four peaks progression in the band is studied in depth, and is found to consist of more than four transitions. By comparing the simulated spectra using the full model and the reduced-dimension 2 states 2 modes models, we characterize those transitions. The origin of the complexities of the spectrum is traced to the C-O nonbonding character of the orbitals that lose electron in the photo-detachment process. Methodology-wise, we derive and present the formalisms for *arbitrary order* expansions of *all* bimodal trigonal Jahn-Teller and pseudo-Jahn-Teller Hamiltonians in vibrational coordinates.

I. INTRODUCTION

Carbon trioxide (CO_3) was proposed to be an intermediate in photoreactions involving CO_2 in 1960s.[1,2] Its existence was confirmed shortly after by IR spectroscopy.[3–5] The molecule is of interest in atmospheric chemistry and astrochemistry. It participates in the quenching of the highly reactive ^1D state of O atom by CO_2.[6] It also participates in the ^{18}O enrichment in CO_2 in the atmospheres of Mars.[7,8] There has been a dispute on its ground state structure symmetry, C_{2v} vs. D_{3h}.[9,10] Recent computational results unanimously pointed to a C_{2v} ground state structure.[11–13] Liu et al. pointed out the hidden-Jahn-Teller[14] origin of this distortion:[12] the strong Jahn-Teller interaction of a high-lying $^1E'$ state generates minima of C_{2v} symmetry in the ground state potential energy surface, and the minima are lower in energy than the $^1A_1'$ state at the undistorted D_{3h} structure. The D_{3h} and C_{2v} structures are separated by a 0.22 eV barrier, which is high enough to let both structures coexist and be spectroscopically observable.[12] Being a member of the $C(CH_2)_{3-n}O_n$ series, the study of CO_3 also provides insight into how the isoelectronic but more electronegative substitution of the peripheral CH_2 groups of trimethylenemethane modifies the electronic structure of this prototypical diradical.[15]

Despite the importance of CO_3, relatively few studies have been dedicated to this molecule, especially when compared to NO_3, which has one more electron and also features rich Jahn-Teller (JT) and pseudo-Jahn-Teller (pJT) interactions.[16–25] Only till two years ago, the first vibronic spectrum of CO_3 was obtained using the negative ion photoelectron (NIPE) spectroscopic technique in a work participated by two of us (B.C. and X.B.W.).[15] Photo-detachment spectrum of the $^2A_2'$ state of CO_3^- was recorded, with transitions to both singlet and triplet manifolds of CO_3. The adiabatic electron affinity and the adiabatic energy gap between the singlet ground state and the lowest triplet state of CO_3 were accurately measured to be 4.06 and 0.77 eV, respectively. In the same study, theoretical simulations were carried out to facilitate the understanding of the complicated NIPE spectrum. The simulations were based on the Born-Oppenheimer (BO) approximation. Under this approximation, the JT effects of the two lowest triplet states, $^3E''$ and $^3E'$, are assumed to be static: (1) within each of the $^3E''$ and $^3E'$ states, the molecular vibrational motion is assumed to be localized at one of the distorted C_{2v} minima of the adiabatic potential energy surface (APES); (2) within each pair of JT-split states, only transitions to the one with low

energy, whose APES has minima, are considered.

This model needs to be improved. First, the previous simulation resulted in a 4 peaks vibrational progression with a 560 cm^{-1} interval, which was assigned to O-C-O bending on the $^3A_1$ APES, the $^3A_1$ being the low-lying state in the JT-splitting of the $^3E'$ term. However, the JT distortion energies (E_{JT}s) of the $^3E''$ and $^3E'$ states, which are the energy differences between the undistorted D_{3h} and the distorted C_{2v} structures, were estimated to be smaller than 3 kcal/mol, which is about 1000 cm^{-1}. The shallow well of ~ 1000 cm^{-1} on the APES can accommodate only one vibrationally excited level with the 560 cm^{-1} fundamental wave number, taking into account the zero point vibrational energy, i.e., $((1 + 1/2) \times 560 = 840 <$ 1000 cm^{-1}). The second and third vibrational excited states, which were supposed to give the third and fourth peaks in the progression, would be higher in energy than the conical intersection. With their vibrational wave packets sampling the conical intersection, the BO approximation, on which the simulation was based, must break down.[26] Second, although the high-lying state of a JT pair does not have a minimum on its APES, it does contribute to the vibronic spectrum. For instance, the Slonczewski resonances arise from excitations to the high-lying state.[27] These two main concerns motivate us to reinvestigate the vibronic spectrum involving the two triplet E-type states, focusing on the dynamic and non-adiabatic nature of their JT and pJT interactions.

Another motivation of this work is methodology-wise. CO_3 is in trigonal symmetry. Yes, the molecule's ground state adopts a C_{2v} structure. However, in terms of vibronic interaction, it is more convenient to consider it as a distortion from the parental D_{3h} symmetry. As this study is dedicated to the JT and pJT effects of a trigonal molecule, we take this opportunity to present the general formalisms of JT and pJT Hamiltonian operators in all 6 trigonal symmetries.

In a JT or pJT problem, the relevant Hamiltonian operator (which can be of a molecule or of a local formation in solid) is represented using a reduced resolution of identity of a set of symmetry-adapted, vibrationally coupled diabatic states.[28,29] The slow variation of the diabatic states with respect to nuclear distortion determines that the resultant Hamiltonian matrix elements can be expanded as Taylor series of symmetry-adapted vibrational coordinates.[30–37] While the expansions are traditionally[38] truncated at the second order and the resultant Hamiltonians can describe JT and pJT interactions to a qualitative accuracy, a growing number of studies, both theoretical and experimental, have shown inadequacies of

the low-order expansions.[17,22,23,38–48]

Motivated by the importance of the high-order expansions, we endeavour to derive general expansion formulas of the JT and pJT Hamiltonian operators up to arbitrary order.[49–52] In Ref. 52, we propose an idea to summarize all bimodal JT and pJT Hamiltonian expansion formulas in one class of axial symmetries (tetragonal there) in a small number of tables: one table of eigenvalues of symmetry operators for independent Hamiltonian matrix elements, $Int\left(n/2\right)+1$ tables of root expansion formulas, and $2\left(Int\left(n/2\right)+1\right)$ tables of constraints that are applied to the root expansions. Here, n indicates the order of the principal symmetry axis (e.g., 4 for tetragonal symmetries) and Int means taking the integer part of its argument. Following the same logic, we have derived expansion formulas for all 908 bimodal JT and pJT Hamiltonians in the 6 trigonal symmetries (C_3, C_{3h}, D_3, C_{3v}, D_{3h}, and D_{3d}) in Section S1 in the Supplementary Information (SI). The formalisms are summarized in Tables S1-S7 ($1+3\left(Int\left(3/2\right)+1\right)=7$). The detailed procedure of obtaining the expansion formulas relevant to the CO_3 JT and pJT problems under consideration is given in Section S2 to demonstrate how to use the presented formalisms. Due to the ubiquity of trigonal JT and pJT problems, the broad applicability of the presented formalisms is evident.

This paper is organized as follows. In Section II, the expansion formulas of the JT and pJT Hamiltonians of interest, the vibronic model, and technical details of the quantum chemistry calculations and quantum dynamic simulations involved are introduced. In Section III, the simulation results of the JT and pJT interactions that give the lowest triplet band of the CO_3^- NIPE spectrum are presented and discussed. Section IV concludes the paper.

II. METHODOLOGIES

A. Vibronic Hamiltonian operator

The vibronic Hamiltonian operator of the JT and pJT interactions of the $^3E''$ and $^3E'$ states take the form of

$$\hat{H}=\hat{T}_N\underline{\underline{1}}_{4\times4}+\begin{pmatrix} H_{X''X''} & H_{X''Y''} & H_{X''X'} & H_{X''Y'} \\ & H_{Y''Y''} & H_{Y''X'} & H_{Y''Y'} \\ & & H_{X'X'} & H_{X'Y'} \\ & & & H_{Y'Y'} \end{pmatrix}. \tag{1}$$

The two real diabatic components of the E-type states are labelled as X and Y. $\hat{T}_N$ is the nuclear kinetic operator for the 6 vibrational degrees of freedom, and it is multiplied to the 4×4 unit matrix in any diabatic representation. In the following electronic Hamiltonian matrix in the diabatic representation, which is a symmetric matrix, only the upper triangle is given. Vibronic coupling is represented by the dependence of those matrix elements on nuclear configurations, i.e., the vibrational coordinates.

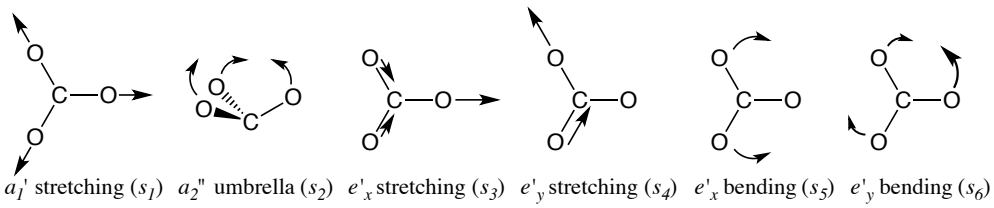

FIG. 1. The six symmetry-adapted internal vibrational modes of CO_3. In the e'_x stretching and the e'_y bending vibration, the motions along the long arrows are twice of those along the short arrows.

The six symmetry-adapted vibrational modes of CO_3 are shown in Figure 1. The irreducible representations (irreps) that they belong to and their coordinates (s_{1-6}) are given below them. Their mathematical expressions in the internal coordinates (bond lengths, bond angles, and the pyramidal angle) are well known (e.g., see Table I in Ref. 53) and are not repeated. The stretching coordinates $s_{1,3,4}$ have length unit, and the pyramidalizing and bending coordinates $s_{2,5,6}$ have angular units. The reference structure with $s_{1-6} = 0$ is the CO_3^- ground state D_{3h} structure optimized at the U-B3LYP/aug-cc-pVTZ level,[54–56] with a 1.272 Å CO bond length. The same basis set is used in all electronic structure calculations in this work, which are performed using the GAMESS-US program package.[57,58]

Adopting a similar approximation as in Ref. 59, each H_{ij} element is expressed as a hierarchical expansion in terms of functions of lower dimensions of the vibrational coordinates:

$$\begin{aligned} H_{ij}(s_{1-6}) = {} & H_{ij}(0) + H_{ij}(s_1) + H_{ij}(s_2, s_3, s_4) + H_{ij}(s_2, s_5, s_6) - H_{ij}(s_2) \\ & + H_{ij}(s_3, s_4, s_5, s_6) - H_{ij}(s_3, s_4) - H_{ij}(s_5, s_6). \end{aligned} \quad (2)$$

$H_{ij}(0)$ is just a quantity obtained at the reference structure, with $H_{i\neq j}(0) = 0$ and $H_{ii}(0)$ being the energies of the E-type states. Due to symmetry, only the diagonal $H_{ii}(s_1) \neq 0$. These diabatic potentials are represented by Morse potential functions (Eq. S3 and Figure S4) and

the double degeneracies of the E-type states remain along s_1. The symmetry-adapted expansion formulas of $H_{ij}(s_2, s_3, s_4)$ and $H_{ij}(s_3, s_4, s_5, s_6)$ are given in Eqs. S9, S14, and S18. They are readily obtained using Tables S1-S7. The convenience of using the presented JT and pJT formalisms, which are correct, complete, and concise, is manifested. $H_{ij}(s_2, s_5, s_6)$ shares the same expansion formula with $H_{ij}(s_2, s_3, s_4)$. $H_{ij}(s_3, s_4)$ and $H_{ij}(s_5, s_6)$ are obtained by setting $s_2 = 0$ in the respective 3-D expansions. $H_{ij}(s_2)$ is obtained by setting $s_3 = s_4 = 0$ in $H_{ij}(s_2, s_3, s_4)$. The subtractions in Eq. 2 are to remove the duplicate terms in the final expansion.

The numerical values of $H_{ij}(s_1)$, $H_{ij}(s_2, s_3, s_4)$, $H_{ij}(s_2, s_5, s_6)$, and $H_{ij}(s_3, s_4, s_5, s_6)$ are obtained by running general multi-configurational quasi-degenerate perturbation theory (GMC-QDPT)[60–62] calculations (averaging all four triplet component states) and diabatizations[34,35,63] on the respective single- and multi-dimensional grids of the vibrational coordinates. The Morse functions and the expansions are then fitted against the numerical data to obtain their parameters. 6-th order expansions are used for the $H_{ij}(s_2, s_3, s_4)$s and $H_{ij}(s_2, s_5, s_6)$s, while 4th order expansions are used for the $H_{ij}(s_3, s_4, s_5, s_6)$s. Some terms are dropped when overfitting occurs. The orders of the expansions are determined by the fitting errors. We stop increasing the order when the fitting error is smaller than or comparable to the 40 meV resolution of the experimental spectrum. Some examples of the fitting errors are shown in Section Section S3. The FORTRAN subroutine that generates the $\underline{\underline{\underline{H}}}$ matrix in Eq. 1 with inputs of s_{1-6} is available upon request.

B. Active spaces and configurations of the relevant states

The active space of the GMC-QDPT calculations for the $H_{ij}(s_{2-6})$s includes all valence π orbitals and O σ lone pair orbitals, and the electrons occupying them (7o10e for CO_3; 7o11e for CO_3^-). These orbitals and the main configurations of the states under consideration are shown in Figure 2. An attempt has been made to include the third lowest-lying triplet state, the $^3A_2'$ state, in the vibronic model to see whether there is any pJT interactions between this state and the two E-type states. The pJT interactions are found to be too weak to make any substantial change in the simulate spectrum of the lowest triplet band, the A band in the notation of Ref. 15. The 7o10e GMC-QDPT calculation shows that the $^3A_2'$ state lies 0.73 and 0.66 eV above the $^3E''$ and $^3E'$ states, respectively. These relatively large

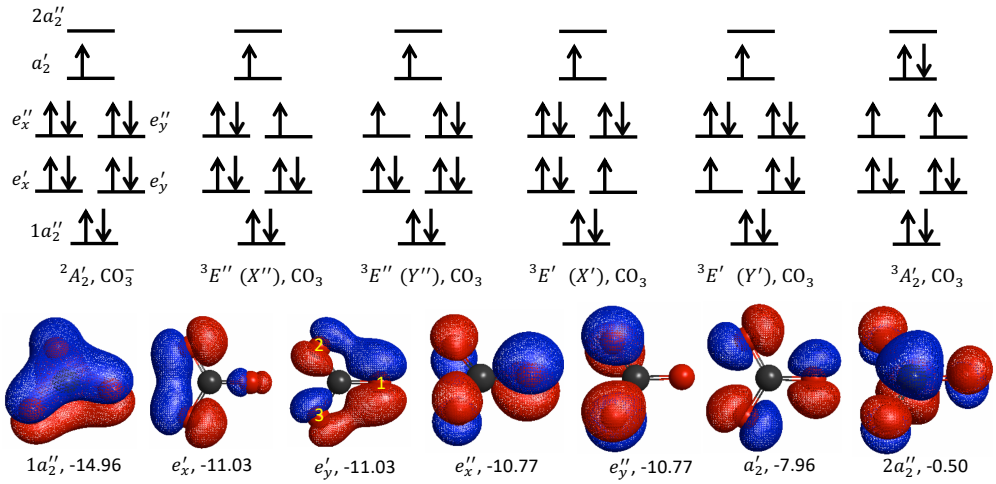

FIG. 2. The active orbitals and the main configurations of the states under consideration. The O atom labels in the e_y' orbital plotting are used for latter discussion. The B3LYP orbital energies in eV calculated at the D_{3h} reference structure for the CO_3 $^1A_1'$ ground state are given under the orbitals.

energy gaps may help prevent significant pJT interactions. More importantly, the $^3E''$-$^3A_2'$ pJT interaction requires an e'' mode, which is absent in CO_3. Symmetry-wise, the $^3E'$-$^3A_2'$ pJT interaction can be induced by the e' modes. However, the two states are coupled by a 2-electron integral, which is relatively less dependent on nuclear configuration distortion than 1-electron integrals. The pJT interaction is hence expected to be small. Actually, for genuine diabatic states that have two different occupied spin orbitals, their pJT interaction is zero.[28] The photo-detachment to the $^3A_2'$ state itself is forbidden, because it involves removing one electron from the e'' shell, and exciting another electron from the e'' to the a_2' orbital. The norm of the Dyson orbital in this two-electron process is zero. Since the $^3A_2'$ state does not contribute to the A band directly or indirectly, it is ignored in the following discussion.

The configurations in the figure show that the photo-detachments to the $^3E''$ and $^3E'$ states mainly occur by removing an electron from the e'' and e' orbitals, respectively. These orbitals feature C-O nonbonding character, as evidenced by their relatively small 0.26 eV difference in B3LYP orbital energies in Figure 2. The change of the CO bond lengths in the photo-detachments is hence not expected to be substantial, leaving the CO σ bonding (antibonding) orbitals more close to be doubly occupied (unoccupied). It is thus reasonable

not to include the C-O σ bonding and nonbonding orbitals in the active space in calculating $H_{ij}\,(s_{2-6})$s. The occupancies of the C-O σ bonding and antibonding orbitals are more fractional along the a_1' CO stretching. Therefore, in the calculations for the $H_{ii}\,(s_1)$s, all valence orbitals and electrons are included in the active space (13o16e for CO_3; 13o17e for CO_3^-).

C. Nuclear kinetic operator

In constructing the kinetic operator $\hat{T}_N$, we follow the same approximation as for PH_3^+ in Ref. 59, i.e.,

$$\hat{T}_N = \frac{1}{2}\underline{\hat{P}}^T\underline{\underline{G}}\underline{\hat{P}}, \tag{3}$$

with $\underline{\hat{P}}$ being a column vector of the conjugate momentum operators of s_{1-6} ($\frac{\hbar}{i}\frac{\partial}{\partial s_k}$) and a constant metric matrix $\underline{\underline{G}}$, whose elements are evaluated at the D_{3h} reference structure and are given in Eq. S19. The constant $\underline{\underline{G}}$ approximation works well for PH_3^+. It is expected to work even better for CO_3, considering that the planar structure is the minimum of all diabatic potentials along s_2, while it is the maximum of the ^2E diabatic potential of PH_3^+. As shown later, the APES derived from the $^3E''$ state has a maximum at the reference structure (Figure 5). However, the two symmetric minima are shallow and are located close to the reference structure. The pyramidal distortion is thus by no means significant. Also, the heavy nuclear masses of the O nuclei (compared to the protons in PH_3^+) help to reduce the distortion from the reference structure.

D. Simulation of the NIPE spectrum using the 4 states 6 modes vibronic model

The vibrational ground state of CO_3^- is obtained by propagating an initial 6-D (s_{1-6}) Gaussian wave packet on the anion's $^2A_2'$ ground state APES in imaginary time. A $100i$ fs propagation is found to be enough to converge to the vibrational ground state. The $^2A_2'$ APES takes the same function form of any of the diagonal $H_{ii}\,(s_{1-6})$s mentioned above, and its parameters (in total 34 parameters) are obtained in a similar way. The same $\hat{T}_N$ with the constant $\underline{\underline{G}}$ matrix is used in the propagation. The resultant adiabatic vibronic state is labelled as $|0\rangle\,|^2A_2'\rangle$ with the 0 indicating the vibrational ground state. The photo-

detachment is simulated by acting the formal dipole operator

$$\hat{\mu} = \mu_{E''} \left(|X''\rangle + |Y''\rangle \right) \left\langle {}^2A_2' \right| + \mu_{E'} \left(|X'\rangle + |Y'\rangle \right) \left\langle {}^2A_2' \right| + h.c. \tag{4}$$

on $|0\rangle \, |^2A_2'\rangle$. *h.c.* stands for hermitian conjugate of the explicitly given part of the operator. This corresponds to the Condon approximation. Associated with this approximation is the assumption that the ejected electron propagate in the totally symmetric s wave. The angular distribution of the photoelectron is beyond the scope of this work and this assumption does not impair our conclusions on the nature of the JT and pJT interactions of the triplet states. The amplitudes of $\mu_{E''}$ and $\mu_{E'}$ for detachments to the $^3E''$ and $^3E'$ states are approximately determined by the norms of the respective Dyson orbitals.[64] Using the GMC-QDPT wave functions of the states at the reference structure, we calculate the Dyson orbitals and their norms, which give the relation $\mu_{E'} = 1.2\mu_{E''}$. We have hence determined the photo-detached vibronic state, $|\Psi(0)\rangle = |0\rangle \left(|X''\rangle + |Y''\rangle + 1.2\,|X'\rangle + 1.2\,|Y'\rangle \right)$ up to a normalization factor. The transition dipole moments are matrix elements between the MOs shown in Figure 2 and scattering waves of the ejected electron, whose values determine the actual $\mu_{E'}/\mu_{E''}$ ratio. The 1.2 obtained using the norms of the Dyson orbitals is an approximate ratio. We treat the ratio as an adjustable parameter around this value. As shown below, the ratio of 1.6 gives a better theory-experiment agreement.

After being normalized, this initial state is propagated in real time using the vibronic Hamiltonian operator in Eq. 1, and its autocorrelation function is calculated,

$$C(t) = \langle \Psi(0) | \, e^{-i\hat{H}t} \, |\Psi(0)\rangle \, . \tag{5}$$

Fourier transform of $C(t)$ gives the simulated vibronic spectrum of the lowest triplet band,

$$I(\omega) = \int_0^\infty C(t) \, e^{i\omega t} g(t) \, dt. \tag{6}$$

The damping function

$$g(t) = \cos\left(\frac{\pi t}{2T}\right) \Theta\left(1 - \frac{|t|}{T}\right) e^{-\Gamma|t|} \tag{7}$$

is multiplied to the integrand to remove the spurious oscillation due to the finite propagation time T and to account for the finite resolution in experiment. Θ is the heaviside step function. $1/\Gamma = 33$ fs is chosen, in accordance with the 40 meV resolution of the NIPE reported in Ref. 15. $T = 500$ fs is chosen and it is found to be enough to converge the simulated spectrum.

All the propagations (both in real and imaginary time) and the Fourier transform are performed using the multi-configurational time-dependent Hartree (MCTDH) program package.[65–67] Vibrational wave packets are expressed using harmonic oscillator type of discrete variable representation (DVR), with the ranges of the coordinates large enough so that the propagated vibronic states have no amplitude near the boundaries. The ranges of s_{1-6}, the numbers of grid points and single particle functions are given in Table S8. The convergences with respect to the numbers of grid points and single particle functions are shown in Figure S7. The least occupied natural orbitals in the MCTDH simulations are small (close to 10^{-3}). For the reduced-dimension ${}^3E'' \otimes e'$, ${}^3E' \otimes e'$, and $({}^3E'' + {}^3E') \otimes a_2''$ models, diagonalizations of the low-dimension vibronic Hamiltonian matrices are performed to obtain the eigenstates and the spectra.

III. RESULTS AND DISCUSSIONS

A. Qualitative understandings of the JT and pJT interactions based on reduced-dimension models

With the knowledge of the eigenstates and eigenenergies of a vibronic Hamiltonian, we can completely decipher the relevant vibronic spectrum. Although it is unrealistic to solve the Schrödinger Equation for the full $({}^3E'' + {}^3E') \otimes (a_1' + a_2'' + e' + e')$ problem, insights into the spectrum can be obtained by considering the JT- and pJT-active vibrational modes individually.

1. The $E \otimes e'$-type problems, with the e' bending mode

We first investigate the ${}^3E'' \otimes e'$ and ${}^3E' \otimes e'$ JT problems, with the e' bending mode. The 1-D cuts of the 4 component states' APESs along s_5 are shown in Figure 3(a). The vertical ${}^3E''$ energy is taken as the 0 reference, and the vertical ${}^3E'$ energy is calculated to be 0.074 eV higher using the 7o10e active space. This small gap is reasonable, as both the e' and the e'' orbitals are mainly C-O nonbonding orbitals. There is some O-O net bonding character in the e' orbitals (more obvious in the e_x' orbital plot in Figure 2) so that their energies are lower than those of the e'' orbitals (Figure 2, again) and it takes extra energy

to remove an electron from this shell. The $^3E'$ state is thus higher in energy.

The $^3E'$ state has a much larger JT distortion energy (E_{JT} = 0.149 eV) than the $^3E''$ state (E_{JT} = 0.003 eV). This difference in E_{JT} is explained by the different O-O bonding/antibonding characters of the e' and e'' orbitals. The e' orbitals (Figure 2), with in-plane O-O bonding and antibonding character, have their energies more sensitive to the in-plane e' bending motion than the e'' π orbitals. For instance, when s_5 changes from 0° to 10°, the e'_x and e'_y orbital energies change by 0.165 and −0.145 eV, while the e''_x and e''_y energies change only by 0.088 and −0.066 eV. These orbital energy changes are obtained from the complete active space self-consistent field (CASSCF) step of the 7o10e GMC-QDPT calculation, not the B3LYP energies shown in Figure 2. We use CASSCF orbital energies here because we can only obtain diabatic molecular orbitals with this method. This inconsistency in method does not blur the trend of the orbital energy variations. With a hole in the e' shell, the $^3E'$ state loses the balance of the stabilization and destabilization of the e' orbitals. Its two component states are hence stabilized and destabilized more substantially than the $^3E''$ counterparts along the e' bending. Please note that along s_5 (and s_3 too), the diabatic states are just reordered at different ranges of the coordinate, instead of being mixed, to give the adiabatic states.

Specifically, in the positive s_5 direction (following the arrows of the e'_x binding mode in Figure 1), the e'_y orbital is stabilized by losing O_2-O_3 σ antibonding character and gaining O_1-O_2 and O_1-O_3 σ bonding character (see the e'_y orbital in Figure 2 and the numbering of the O atoms there). Oppositely, the e'_x orbital loses O_2-O_3 (gains O_1-O_2 an O_1-O_3) σ bonding (antibonding) character and is destabilized. It is thus the $|Y'\rangle$ state that has a singly occupied e'_x and a doubly occupied e'_y orbital that forms the low-lying adiabatic state in the positive s_5 direction, while the $|X'\rangle$ component with the opposite occupation scheme in the e' shell forms the high-lying adiabatic state. In the negative s_5 direction, the energy ordering of the two component states is reversed.

For the $^3E''$ state, it is the $|X''\rangle$ ($|Y''\rangle$) component state with a doubly occupied e''_x (e''_y) and a singly occupied e''_y (e''_x) orbital forms the low-lying adiabatic state in the positive (negative) s_5 direction. This is contradictory to the expectation based on the fact that the e''_x (e''_y) orbital is destabilized (stabilized) in the positive s_5 direction, since the former features O_1-$O_{2,3}$ antibonding character and O_2-O_3 bonding character, while the latter features O_2-O_3 antibonding character only. However, these π O-O bonding and antibonding characters are

weaker than the σ counterparts in the e' orbitals. Consequently, the small orbital energy changes do not dominate the component states' energy changes along the bending motion.

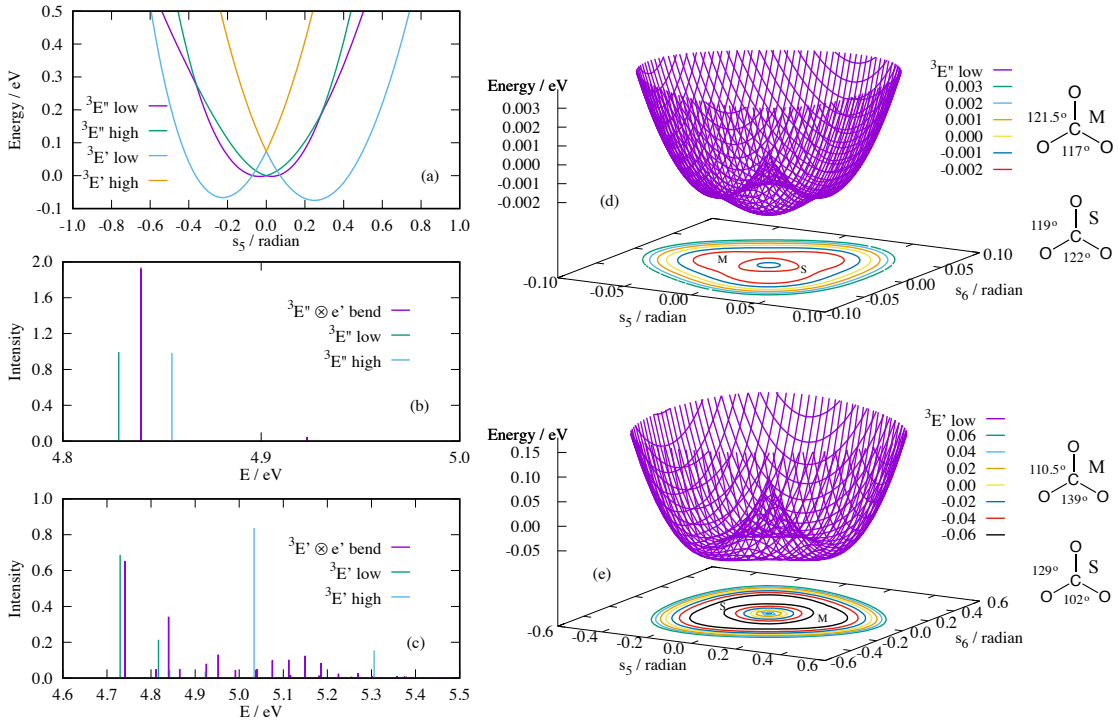

FIG. 3. (a) The 1-D cuts of the adiabatic potential energy surfaces derived from the $^3E''$ and $^3E'$ states along s_5; (b) comparison of the calculated $^3E'' \otimes e'$ vibronic spectrum with the e' bending mode and those obtained based on the BO approximation; (c) the same as (b) but for the $^3E'$ state; the low-lying APESs of the (d)$^3E'' \otimes e'$-bending problem and (e) the $^3E' \otimes e'$-bending problem. The vertical $^3E''$ energy is taken as the reference zero energy in (a), (d), and (e). The CO_3^- e'-bending ground state energy is taken as the reference zero energy in (b) an (c). The minimum energy troughs are between the two red contour lines in (d) and between the two black contour lines in (e). The C_{2v} minima and saddle points are indicated by "M" and "S", respectively. Their bond angles are shown beside the APESs. Please note the three-fold symmetries of the APESs and there are hence three symmetry-connected minima and three saddle points within each panel.

Figure 3(a) also shows that the two minima on the positive and negative s_5 of each of the low-lying $^3E''$ and $^3E'$ APESs are close in energy. They only differ by 0.0006 eV and 0.0083 eV, respectively, in the $^3E''$ and $^3E'$ APESs. The full 3-D plots of the APESs are given in Figures 3(d) and (e). The two minima correspond to two C_{2v} structures, one is a true minima on the s_5-s_6 2-D space while the other a saddle point.[28] The C_{2v} structures are shown beside

the APESs. Due to the trigonal symmetry, there are three such minima and three such saddle points on the 2-D space and they are connected by a trough on the APES, on which the pseudo-rotation on the s_5-s_6 plane occurs. The < 0.01 eV barrier is unlikely to statically trap the configuration in one of the C_{2v} minima, which is the assumption made in Ref. 15 in simulating the A band of the CO_3^- NIPE spectrum. The almost barrier-less trough allows hinder-less pseudo-rotation around the conical intersection, resulting in significant geometric phase effects.[68–72] One consequence is that the vibronic ground state of this JT problem is an E-type doubly degenerate state (*vide infra*),[73,74] instead of an A-type non-degenerate state, which is anticipated based on the BO approximation. All these features of the APESs determine the dynamic nature of the JT effects of the two E states, which are far beyond structural distortion. Another interesting observation in Figure 3(a) is the crossing of the $^3E''$ and $^3E'$ APESs around the minimum of the former. This low-lying degeneracy indicates a significant vibronic coupling between the two states through the a_2'' umbrella mode, which further complicates the CO_3^- NIPE spectrum.

The comparisons of the simulated spectra obtained using the $E\otimes e'$-type JT models (fully vibronic) and those obtained based on the BO approximation (adiabatic) directly manifest the dynamic and non-adiabatic nature of the e' bending associated to the $^3E''$ and $^3E'$ states. The comparisons are shown in Figures 3(b) and (c) for the $^3E''$ and $^3E'$ states, respectively. The energies in the abscissas correspond to the detachment energies to the triplet manifolds with all modes other than the e'-bending are frozen. The intensities are estimated as the modular square of the overlap between the e' bending vibrational functions of the anion's ground state and those of the JT vibronic eigenstates. The energies, irreps, and transition intensities of the lowest 10 vibronic eigenstates (counting each of the E-type component state) of the reduced-dimension models are listed in Table 1. 10 states are enough to show the energetic relations between eigenstates of E- and A-type irreps, which are of interest.[24,73] Due to the Condon approximation and the symmetry of the transition dipole operator in Eq. 4, only states of E'' and E' irreps have nonzero intensities.

The difference between the fully vibronic and adiabatic spectra is obvious. By "adiabatic spectra", we mean the spectra obtained assuming vibrational motions to occur on separate APESs without geometric phase correction and diagonal BO correction. For the $^3E''$ state (Figure 3(b)), there is only one significant transition to the ground vibronic state, which is of E'' irrep. The double degeneracy of this state is reflected by the close to 2 intensity,

TABLE 1. The lowest 10[a] vibronic eigenstates of the $E \otimes e'$-type reduced-dimension models: their energies, symmetries, and intensities in NIPE spectrum

$^3E'' \otimes e'$-bending			$^3E'' \otimes e'$-stretching		
Energy / eV (cm^{-1})	Symmetry	Intensity[b]	Energy / eV (cm^{-1})	Symmetry	Intensity[b]
4.839 (0)	E''	0.9643	4.806 (0)	E''	0.8411
4.913 (597)	A_1''	0	4.934 (1032)	A_1''	0
4.923 (678)	E''	0.0224	5.025 (1766)	E''	0.1304
4.926 (702)	A_2''	0	5.028 (1791)	A_2''	0
4.993 (1242)	E''	0.0033	5.129 (2605)	E''	0.0092
5.002 (1315)	A_2''	0	5.198 (3162)	A_1''	0
5.006 (1347)	A_1''	0	5.230 (3420)	E''	0.0164
$^3E' \otimes e'$-bending			$^3E' \otimes e'$-stretching		
Energy / eV (cm^{-1})	Symmetry	Intensity[b]	Energy / eV (cm^{-1})	Symmetry	Intensity[b]
4.741 (0)	E'	0.3265	4.878 (0)	E'	0.8004
4.765 (194)	A_2'	0	4.993 (928)	A_1'	0
4.777 (290)	A_1'	0	5.089 (1702)	A_2'	0
4.811 (565)	E'	0.0244	5.091 (1718)	E'	0.1481
4.840 (798)	E'	0.1710	5.183 (2460)	E'	0.0106
4.865 (1000)	E'	0.0248	5.253 (3025)	A_1'	0

[a] Counting each E-type component state. [b] The tabulated intensities of E'' and E' vibronic states are for each of the doubly degenerate components. They are multiplied by 2 in Figures 3(b),(c) and Figures 4(b),(c).

as the transition dipole moment from the $^2A_2'$ to each of the E component states has been taken to be 1. Such a one peak spectrum is consistent with the small magnitudes of E_{JT} and bending distortion of the $^3E''$ state shown in Figure 3(a). This degenerate transition splits to two peaks in the BO approximation, corresponding to the transitions to the lowest vibrational states on the two $^3E''$ APESs. This degenerate ground vibronic state is 0.073 eV lower in energy than the following non-degenerate state, which is of A_1'' irrep (Table 1).

The lack of triply degenerate ground vibronic state is a direct evidence of the incapability of the barriers in the minimum energy trough to trap the configuration at one of the C_{2v} minima.[24,28,73] The dynamic nature of the JT problem is evident.

The fully vibronic energy levels also indicate the non-adiabatic nature of the JT problem. If the JT problem is only dynamic but adiabatic, i.e., that the vibrational motion remains on one APES although it samples all three minima, the eigenenergies must follow the pattern of

$$E\left(E\right) < \left(E\left(A_1\right), E\left(A_2\right)\right) < E\left(E\right) < \left(E\left(A_1\right), E\left(A_2\right)\right) \cdots , \tag{8}$$

i.e., alternating energy levels of one E-type and two A-type states. The orderings of the A_1- and A_2-type states is uncertain.[73] This pattern is obviously not followed by the eigenenergies of the ${}^3E'' \otimes e'$-bending problem in Table 1. The non-adiabatic nature of the JT problem is evident. Please note that the non-degeneracy between the A_1- and A_2-type vibronic eigenstates in Table 1 does not indicate large barriers on the minimum energy trough. Whenever the minimum energy trough is non-circular, i.e., the vibronic angular momentum is not conserved, the A_1-A_2 degeneracy is lifted. Figures 3(d),(e) and 4(d),(e) clearly show non-circular minimum energy troughs for the reduced-dimension $E \otimes e'$-type problems.

For the ${}^3E'$ state (Figure 3(c)), there are more peaks in the fully vibronic and adiabatic spectra. This is consistent with the state's more significant JT coupling shown in Figure 3(a). The peak of the lowest fully vibronic state and the peak of the lowest state in the BO approximation are seen at similar energy. This is typical for large JT coupling, for which the vibrational motion of the ground vibronic state is mainly confined to the minimum energy trough.[26,28] However, the former arises from the doubly degenerate vibronic state of E' irrep, while the latter a non-degenerate A_1' vibronic state. For the fully vibronic model, the E' vibronic ground state is 0.024 eV lower in energy than the following non-degenerate A_2' state (Table 1); again, there is no static configuration confinement at one of the C_{2v} minima. As the energy increases, the vibrational motion is more likely to sample the conical intersection and the fully vibronic becomes more different from the adiabatic spectrum. The non-adiabaticity of the ${}^3E' \otimes e'$-bending JT coupling is corroborated by the energy levels shown in Table 1. The first four levels follow the pattern in Eq. 8, and can be understood as arising from vibrational motion on the ${}^3E'$ deep low-lying APES. However, this pattern does not continue into the following two E' levels, in which the vibrational motion has enough

energy to sample the conical intersection and thus is not confined on one APES.

2. The $E \otimes e'$-type problems, with the e' stretching mode

Similar analysis of APESs and comparisons of fully vibronic and adiabatic spectra are performed for the two $E \otimes e'$-type reduced-dimension problems, with the e' stretching mode. The results are presented in Figure 4 and the respective lowest 10 energy levels are included in Table 1. Similar E_{JT}s are obtained for the two states, 0.027 eV for $^3E''$ and 0.025 eV for $^3E'$. Apparently, the e'_x and e''_x orbitals are stabilized through gaining O_2-O_3 bonding and losing O_1-$O_{2,3}$ antibonding character in the positive s_3 direction (following the arrows of the e'_x stretching mode in Figure 1), while the e'_y and e''_y orbitals are destabilized. In consistence with this trend, the $|X'\rangle$ component state with the $(e'_x)^2 \left(e'_y\right)^1$ occupation forms the low-lying adiabatic state in the positive s_3 direction, while the $|Y'\rangle$ component state with the $(e'_x)^1 \left(e'_y\right)^2$ occupation forms the low-lying adiabatic state in the negative s_3 direction. Note that the e'_x stretching does not affect the overlaps of the O in-plane p orbitals as much as the e'_x bending. Correspondingly, the $^3E'$ E_{JT} is 5 times smaller in the stretching than in the bending. The energy ordering of the $^3E''$ components, however, is opposite again to the prediction based on the orbital energy changes. The $|Y''\rangle$ ($|X''\rangle$) component is lower in the positive (negative) direction. This inconsistence is attributed to the inclusion of dynamic correlation effect, which dominates over the variation of the orbital energies. The components do follow the predicted energy ordering at the complete active space configuration interaction (CAS-CI) level. The inconsistence emerges only when the dynamic correlation is introduced at the GMC-QDPT level.

The energy differences between the minima on the positive and negative s_3 direction are 0.011 eV for both the low-lying APESs of the two E-type states. They are slightly larger than the counterparts for the e' bending. However, they are still small and are unlikely to statically trap the structure at the C_{2v} minima in the positive s_3 direction. Hinder-less pseudo-rotations on the minimum energy troughs are anticipated. The full 3-D plots of the low-lying APESs are given in Figures 4(d) and (e), where the minimum troughs are clearly seen. The crossings between the high-lying $^3E''$ APES and the low-lying $^3E'$ APES at the minimum trough of the former shown in Figure 4(a) also indicates their non-adiabatic vibronic coupling through the a''_2 mode.

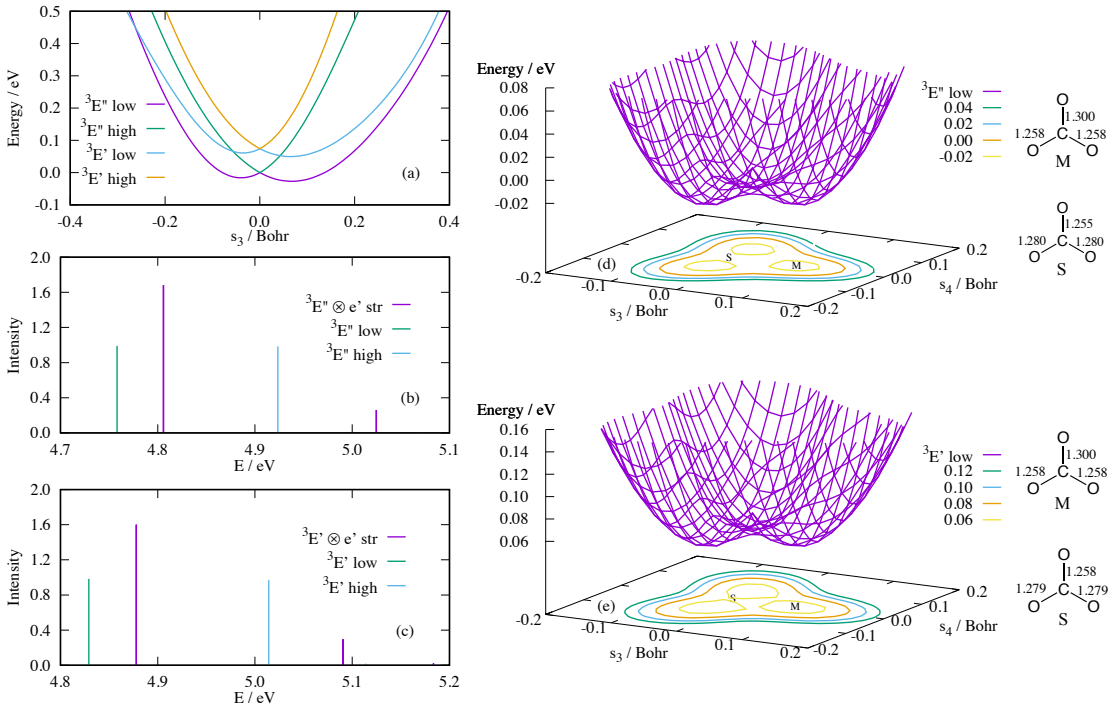

FIG. 4. (a) The 1-D cuts of the adiabatic potential energy surfaces derived from the ${}^3E''$ and ${}^3E'$ states along s_3; (b) comparison of the calculated ${}^3E'' \otimes e'$ vibronic spectrum with the e' stretching mode and those obtained based on the BO approximation; (c) the same as (b) but for the ${}^3E'$ state; the low-lying APESs of the (d)${}^3E'' \otimes e'$-stretching problem and (e) the ${}^3E' \otimes e'$-stretching problem. The vertical ${}^3E''$ energy is taken as the reference zero energy in (a), (d), and (e). The e' stretching ground state energy of the CO_3^- ${}^2A_2'$ state is taken as the reference zero energy in (b) an (c). The minimum energy troughs pass through the three yellow contour circles in both panels. The C_{2v} minima and saddle points are indicated by "M" and "S", respectively. Their bond lengths in Å are shown beside the APESs. Please note the three-fold symmetries of the APESs and there are hence three symmetry-connected minima and and three saddle points within each panel.

The differences between the fully vibronic simulated spectra and the adiabatic ones are evidently shown in Figure 4(b) and (c). The energies in the abscissas correspond to the photo-detachment energies to the triplet manifolds with all modes other than the e' stretching are frozen. They can be compared with the energies in Figures 3(b) and (c). As shown in Table 1, the ground states of the two $E \otimes e'$-stretching JT problems are both doubly degenerate, with their energies 0.13 and 0.12 eV lower than the following non-degenerate A_1'' and A_1' vibronic states in the ${}^3E''$ and ${}^3E'$ cases, respectively. This again reflects the ab-

sence of static configuration confinement at one of the C_{2v} minima and the dynamic nature of the JT problems. The levels of the vibronic eigenstates do not follow the pattern in Eq. 8 and manifests the non-adiabatic nature of the JT problems. The similar spectral profiles in Figures 4(b) and (c) are consistent with the parallel relation between APESs of the $^3E''$ and $^3E'$ states in Figure 4(a).

From these reduced-dimension $E \otimes e'$-type problems, we can safely conclude that the static and adiabatic JT picture of CO_3 being trapped at one of the C_{2v} minima of the triplet states is inapplicable. The inclusion of more modes in the JT problems generally lowers the energies of the conical intersections, since now they can relax their energies along the respective degenerate seams of the $^3E''$ and $^3E'$ states.[26] Also, more conical intersections appear after we consider the $^3E''$-$^3E'$ coupling, i.e., the crossings of the two states' APESs in Figures 3(a) and 4(a). These two aspects increase the non-adiabaticity of the vibrational motions of the two triplet states.

3. *The* $\left(^3E'' +^3 E'\right) \otimes a_2''$ *problem*

To have a sketchy picture of the strength of the pJT interaction between the $^3E''$ and $^3E'$ states, we also look into the $(^3E'' +^3 E') \otimes a_2''$ reduced-dimension pJT problem. The results are shown in Figure 5. The a_2'' umbrella mode is the only vibration that couples the two states. In Figure 5(a), we clearly see that this pJT interaction softens the low APES in comparison to the $^3E''$ diabatic energy surface, so that it has two shallow minima at $s_2 = \pm 0.03$ radian. The conversion of the stationary point at $s_2 = 0$ from a minimum to a maximum indicates a strong pJT interaction. Correspondingly, the high APES is hardened.

The fully vibronic simulated spectrum of this pJT interaction is shown in Figure 5(b). $\mu_{E'} = 1.2\mu_{E''}$ is used in the simulation. For the bright states in the fully vibronic model, their intensity arise either from $\mu_{E''}$ or $\mu_{E'}$, but never together. This is because the two states are coupled by terms with odd powers of s_2. Therefore, within a fully vibronic eigenstate, if the vibrational function multiplied to $^3E''$ is s_2-even and has a nonzero Franck-Condon factor with the CO_3^- vibrational ground state, the vibrational function multiplied to $^3E'$ must be s_2-odd, giving no contribution to the state's intensity. And vice versa. We hence label the peaks of the fully vibronic spectrum using purple and green colours to indicate their intensities arising from $\mu_{E''}$ and $\mu_{E'}$, respectively. There are three such peaks that

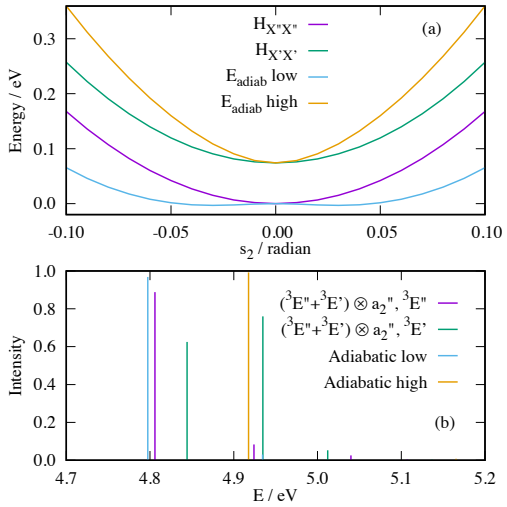

FIG. 5. (a) The 1-D cuts of the diabatic potential energy surface of the ${}^3E''$ an ${}^3E'$ states and the APESs derived from their pJT interaction along s_2 (the coupling between the two states are shown in Figure S8); (b) comparison of the calculated $\left({}^3E'' + {}^3E'\right) \otimes a_2''$ vibronic spectrum and those obtained based on the BO approximation. The vertical ${}^3E''$ energy is taken as the reference zero energy in (a). The a_2'' umbrella vibrational ground state energy of the CO_3^- ${}^2A_2'$ state is taken as the reference zero energy in (b).

have substantial intensities. In contrast, there is only one intense peak in each of the two spectra for transitions to the low and high adiabatic states.

Clearly, even without the e' distortions, the a_2'' umbrella mode has induced a non-adiabatic pJT interaction between the ${}^3E''$ and ${}^3E'$ states. As mentioned above, when the crossings of the ${}^3E''$ and ${}^3E'$ APESs along the e' distortions are considered, the ${}^3E''$-${}^3E'$ coupling is more non-adiabatic. This is just a manifestation of the multimode effect in enhancing non-adiabaticity.[26] Given the dynamic and non-adiabatic nature of the JT and pJT effects in the triplet states, and the mode-mode combination in enhancing the non-adiabaticity, it is necessary to study the A band of the NIPE spectrum using the fully vibronic model that include all the JT- and pJT-active modes.

B. Simulation of the A band using the 4 states 6 modes model

We then use the full vibronic models that include all 4 states (counting each component state) and all 6 vibrational modes (counting each component mode) to simulate the A band

of the CO_3^- NIPE spectrum. The results are shown in Figure 6(a), in comparison with the experiment. The comparison for the low photon energy portion of the spectrum from 4.8 to 5.0 eV, for which the vibronic model is expected to be more accurate, is given in Figure S9. In addition to the $\mu_{E'} = 1.2\mu_{E''}$ obtained from the Dyson orbital calculation, we also use $\mu_{E'} = 1.6\mu_{E''}$ for comparison. Using the 13o17e and 13o16e active spaces for the anion and the neutral molecule, respectively, we calculate the vertical photo-detachment energy from the $^2A_2'$ state to the $^3E''$ state to be 4.83 eV. Subtracting the 0.32 eV zero point vibrational energy of the anion, which is obtained from the imaginary time propagation, and adding the 0.24 eV energy of the first peak in the simulated A band relative to the vertical $^3E''$ energy, the photo-detachment energy that gives the first A band peak is estimated to be 4.75 eV, which is in satisfactory agreement with the 4.83 eV experimental value.

In Figure 6, we slightly shift the simulated A band by 0.08 eV so that its first peak is aligned with the first A band peak in the experiment. The simulated and experimental bands span a similar range of energy. According to Ref. 15, the most significant feature of the experimental spectrum is the progression of 560 cm^{-1} in the first four peaks, which are highlighted by the calibrator in the figure (also see Figure 1 of Ref. 15). We label the four peaks in the simulated spectrum that correspond to the progression by their intervals, which are smaller but not far from 560 cm^{-1}. Considering the complexity of the problem and the model, this error is acceptable. In fact, with the amplification of the the experimental spectrum, we can see that there are more than 4 peaks in this range of energy. For instance, there is a shoulder peak on the red side of the second progression peak, which is highlighted by a red circle in Figure 6(a). In our simulation, this transition has a more pronounced intensity but is at the right position. Overall, the 560 cm^{-1} progression should be viewed as a simplification of the spectrum. Our simulation cannot reproduce some of the fine structures in the "progression". There are two peaks around 4.95-4.98 eV and another two peaks around 5.01-5.05 eV in the experimental spectrum, while the simulation gives only one in each of the respective energy ranges.

The intensities of the transitions are likewise interesting. Using $\mu_{E'} = 1.2\mu_{E''}$ in the simulation, the 510 peak is much more intense than the 0 peak. Their intensities are closer and are more comparable to the experiment when $\mu_{E'} = 1.6\mu_{E''}$ is used. At the D_{3h} reference structure, the GMC-QDPT wave functions are identical to the reference states obtained in the preparatory CAS-CI calculation, i.e., there is no dynamic correlation correction to the

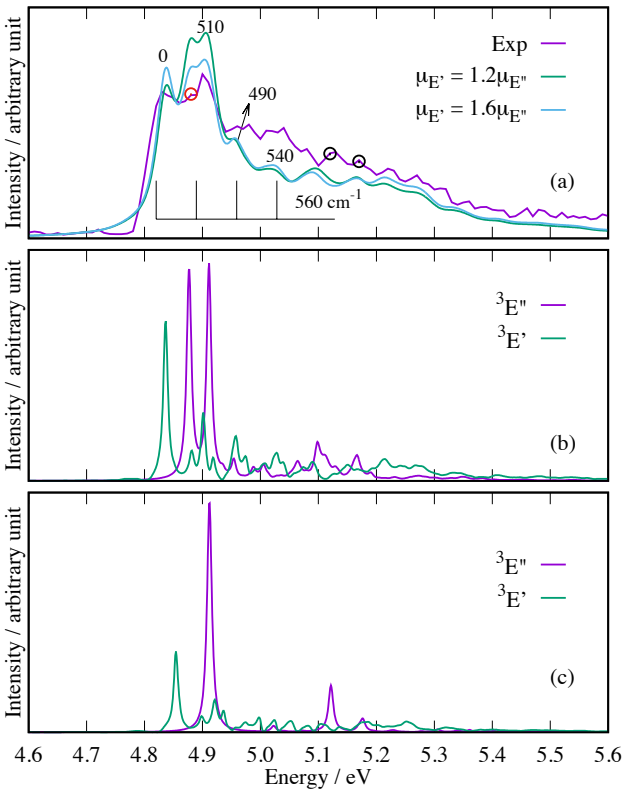

FIG. 6. (a) Simulated A band of the NIPE spectrum using two different ratios of the transition dipole moments to the two triplet states, in comparison with the experimental spectrum; (b) decomposition of the simulated spectrum to contributions of the two triplet states; (c) similar to (b) but with the a_2''-induced $^3E''$-$^3E'$ coupling being turned off. The numbers in (a) by the peaks are the energy intervals (in cm^{-1}) between the denoted peaks and the previous denoted peaks in the simulated spectra.

wave functions. The Dyson orbitals obtained using the wave functions may not give accurate enough intensities.

Both the μ ratios give the 490 and 540 simulated peaks with too low intensities compared to the experiment. One possible reason for this inconsistence is the negligence of the contribution of singlet states to the A band. Our 7o10e calculation shows that at the reference structure, the lowest singlet excited state of CO_3 is a $^1E''$ state, lying 1 eV above the $^1A_1'$ ground state (compared to 0.97 eV reported in Ref. 12). The $^1E''$ state shares a similar electronic configuration with the $^3E''$ state, with a spin-flipping. Adding the 1 eV to the 4.08 eV maximum peak of the X band of the NIPE spectrum, which arises from photo-detachment to the $^1A_1'$ ground state (here we just use the D_{3h} irrep symbol for convenience, knowing that

it actually adopts a C_{2v} structure), we can roughly estimate the vertical photo-detachment to the $^1E''$ state occurs at 5.08 eV. The JT interaction of the $^1E''$ state may give vibronic states that contribute to the NIPE signals around 5.0 eV, where the 490 and 500 peaks are located. In addition to enhancing the intensities, the $^1E''$ state may be responsible for the missing fine structures mentioned above in this range of energy. In short, contrary to the original assignment, the A band should not purely arise from the triplet states. The $^1E''$ state's contribution to this band is an interesting subject for a future study.

To decompose the contributions of the $^3E''$ and $^3E'$ states to the A band, we perform two simulations with $\mu_{E''}$ and $\mu_{E'}$ being set to 0, respectively. The results are shown in Figure 6(b). $1/\Gamma = 132$ fs is used in the damping function $g(t)$ (Eq. 7) to enhance the resolution of the spectra to 10 meV, so that we can have a better idea of how many transitions are hidden under the broad peaks in Figure 6(a). Similar simulations are carried out with the a_2''-mode-induced $^3E''$-$^3E'$ coupling being turned off, so that we can probe the role of the pJT interaction. The results are shown in Figure 6(c). As anticipated, the lowest 0 peak arises from the $^3E'$ state, which gives the lowest energy along the e' bending in Figure 3(a). Comparing the relative positions of the peaks in the fully vibronic simulated spectra of the $E \otimes e'$-type reduced models in Figures 3(b),(c) and 4(b),(c), it is natural to associate the 0 peak to the ground states of the $^3E' \otimes e'$-bending and -stretching JT interactions. Please note that the separate ground states of the 2 reduced-dimension models combine to contribute to the same ground state of the full model.

The 510 peak and its shoulder peak on the red side mainly arise from transitions to the $^3E''$ state, i.e., the combination of the ground states of the $^3E'' \otimes e'$-bending and -stretching JT interactions. The $^3E'$ state also contribute to those two peaks around 4.9 eV. These contributions are likely to arise from the $^3E' \otimes e'$-bending excited states that give the purple peaks between 4.8 and 4.9 eV in Figure 3(c). The comparison of Figures 6(b) and (c) shows that the $(^3E'' +^3 E') \otimes a_2''$ coupling splits the intense transition to the ground vibronic state of $^3E''$ to the 510 peak and the shoulder peak. Without the pJT interaction, there would certainly be no such a shoulder peak.

The 490 and 540 peaks consist of more (but not overwhelmingly) $^3E'$ contributions. It is difficult to characterize them more than saying that they contain the $^3E' \otimes e'$-stretching excited state shown as the second purple peak in 4(c). The purple peak is located 0.2 eV higher than the ground state purple peak, which is consistent with the positions of the 490

and 540 peaks relative to the 0 peak. The comparison of Figures 6(b) and (c) indicates that the $^3E''$ contributions to these two peaks arise from the pJT interaction. The two $^3E''$ peaks at 5.1-5.2 eV can be associated to the $^3E'' \otimes e'$-stretching excited state that gives the purple peak at 5.02 eV in Figure 4(b). This state is split to two transitions when the two sets of e' modes are considered together. They are likely to contribute to the two peaks highlighted by black circles in Figure 6(a).

Overall, the comparison of the two panels in Figure 6 shows a typical feature of non-adiabatic JT vibronic spectra, that "most peaks ... are accumulations of lines rather than single vibronic lines."[26] For instance, recalling each transition to an eigenstate of the vibronic Hamiltonian can only be induced by either the $^3E''$ or the $^3E'$ contribution to that state, we count 6 bright states (2 purple peaks an 4 green peaks) in 4.80-4.92 eV in Figure 6(b). Altogether, they give three peaks, the 0 peak, the 510 peak, and its shoulder peak, in Figure 6(a).

The intercalation of the $^3E''$ and $^3E'$ contributions to the spectrum originate from: (1) the small energy gap between the vertical photo-detachment energies of the two states ($^3E'$ higher by 0.074 eV); (2) the more significant JT distortion of the $^3E'$ state that reverses the energy ordering set by the small gap. The original understanding of the apparent 560 cm^{-1} progression as e'-bending progression on a single triplet state APES is certainly an oversimplification. We mention in passing that the a_1' stretching mode is a spectator for the A band transitions (see Figure S10). This is again due to the mainly C-O nonbonding character of the e' and e'' orbitals. Removing electrons from them does not alter the CO bond lengths substantially. Actually, the Morse potentials of the two states along s_1 have their minima shifted only by 0.021 Å from the minimum of the potential of the anion. This is equal to only a $(0.021/\sqrt{3} =)$ 0.012 Å increase in the CO bond lengths.

IV. CONCLUSIONS

In this work, we have made two contributions. First, we have derived the general expansion formulas for all bimodal Jahn-Teller and pseudo-Jahn-Teller Hamiltonian operators in all the 6 trigonal symmetries. In total, 908 problems are covered, and the formulas can be easily extended to handle problems that involve more than two modes. The formalisms are summarized in 7 tables. They are correct, complete, concise, and convenient to use. Second,

we employ the formulas and perform multi-reference perturbation theory calculations to develop a 4 states 6 modes fully vibronic model to study the Jahn-Teller and pseudo-Jahn-Teller interactions of the $^3E''$ and $^3E'$ states of CO_3, the molecule's triplet manifold with the lowest energy. The reduced-dimension models with only the e' bending or stretching mode are employed to investigate the Jahn-Teller interactions of the two E-type states, which are found to be of dynamic and non-adiabatic nature. A reduced model with only the a_2'' umbrella mode reveals the non-adiabatic nature of the pseudo-Jahn-Teller interaction between the $^3E''$ and $^3E'$ states. All these are explained by the fact that the e' and e'' orbitals from which an electron is extracted are mainly C-O nonbonding orbitals, so that the Jahn-Teller distortion energies are in general not large. Also, the barriers on the minimum energy trough of the adiabatic potential energy surfaces of the Jahn-Teller problems are so small that the e' bending and stretching modes can dynamically sample all three minima of C_{2v} symmetry.

Using the 4 states 6 modes model Hamiltonian operator and quantum molecular dynamics method, we simulate the A band of the negative ion photoelectron spectrum of CO_3^-, which has been assigned to transitions to the $^3E''$ and $^3E'$ states. The simulated spectrum is in satisfactory agreement with the experiment. The apparent 4 peaks progression with a 560 cm^{-1} interval in the experimental spectrum is largely reproduced. Consistent with the dynamic and non-adiabatic nature of the Jahn-Teller and pseudo-Jahn-Teller interactions, this progression cannot be described as transitions to different vibrational states on a single adiabatic potential energy surface. Indeed, it consists of more than four transitions, and the transitions are induced intercalatedly by the contributions of the $^3E''$ and $^3E'$ states to the transition dipole moment. By comparing the reduced-dimension simulated spectra and the full spectrum, we characterize the transitions in the progression. Our calculations also point out the possible contributions of the lowest singlet excited state, the $^1E''$ state, to the A band. We hope that this work will stimulate more studies in the vibronic interactions of CO_3, which is similar to the popular NO_3 and is of importance in atmospheric chemistry and astrochemistry.

V. ACKNOWLEDGEMENTS

T.Z. thanks Carleton University for the start-up grant (186853) and the Natural Sciences and Engineering Research Council (NSERC) of Canada for funding (RGPIN-2016-06276).

X.B.W. thanks the US Department of Energy (DOE), Office of Science, Office of Basic Energy Sciences, the Division of Chemical Sciences, Geosciences, and Biosciences for generous support. We thank the Mark Gordon Group (Iowa State University) for their support of the GAMESS-US program package.

[1] D. Katakis and H. Taube, *J. Chem. Phys.*, 1962, **36**, 416–422.

[2] A.-Y. Ung and H. I. Schiff, *Can. J. Chem.*, 1966, **44**, 1981–1991.

[3] N. G. Moll, D. R. Clutter and W. E. Thompson, *J. Chem. Phys.*, 1966, **45**, 4469–4481.

[4] E. Weissberger, W. H. Breckenridge and H. Taube, *J. Chem. Phys.*, 1967, **47**, 1764–1769.

[5] M. E. Jacox and D. E. Milligan, *J. Chem. Phys.*, 1971, **54**, 919–926.

[6] R. I. Kaiser and A. M. Mebel, *Chem. Phys. Lett.*, 2008, **465**, 1–9.

[7] M. H. Thiemens, T. L. Jackson and C. A. M. Brenninkmeijer, *Geophys. Res. Lett.*, 1995, **22**, 255–257.

[8] A. A. Fedorova, E. Lellouch, D. V. Titov, T. de Graauw and H. Feuchtgruber, *Planet. Space Sci.*, 2002, **50**, 3–9.

[9] C. S. Jamieson, A. M. Mebel and R. I. Kaiser, *ChemPhysChem*, 2006, **7**, 2508–2513.

[10] B. Sivaraman, B. N. Raja Sekhar, D. Fulvio, A. Hunniford, B. McCullough and M. E. Palumbo, *J. Chem. Phys.*, 2013, **139**, 074706.

[11] T. Kowalczyk and A. I. Krylov, *J. Phys. Chem. A*, 2007, **111**, 8271–8276.

[12] Y. Liu, I. B. Bersuker, W. Zou and J. E. Boggs, *J. Chem. Theory Comput.*, 2009, **5**, 2679–2686.

[13] F. Grein, *J. Chem. Phys.*, 2013, **138**, 204305.

[14] I. B. Bersuker, *Chem. Rev.*, 2013, **113**, 1351–1390.

[15] D. A. Hrovat, G.-L. Hou, B. Chen, X.-B. Wang and W. T. Borden, *Chem. Sci.*, 2016, **7**, 1142–1150.

[16] E. Hirota, K. Kawaguchi, T. Ishiwata and I. Tanaka, *J. Chem. Phys.*, 1991, **95**, 771–775.

[17] A. Weaver, D. W. Arnold, S. E. Bradforth and D. M. Neumark, *J. Chem. Phys.*, 1991, **94**, 1740–1751.

[18] J. F. Stanton, *J. Chem. Phys.*, 2007, **126**, 134309.

[19] S. Faraji, H. Köppel, W. Eisfeld and S. Mahapatra, *Chem. Phys.*, 2008, **347**, 110–119.

[20] J. F. Stanton and M. Okumura, *Phys. Chem. Chem. Phys.*, 2009, **11**, 4742–4744.

[21] J. F. Stanton, *Mol. Phys.*, 2009, **107**, 1059–1075.

[22] W. Eisfeld, O. Vieuxmaire and A. Viel, *J. Chem. Phys.*, 2014, **140**, 224109.

[23] T. Codd, M.-W. Chen, M. Roudjane, J. F. Stanton and T. A. Miller, *J. Chem. Phys.*, 2015, **142**, 184305.

[24] W. Eisfeld and A. Viel, *J. Chem. Phys.*, 2017, **146**, 034303.

[25] A. Viel and W. Eisfeld, *Chem. Phys.*, 2018, **509**, 81–90.

[26] H. Köppel, W. Domcke and L. S. Cederbaum, *Adv. Chem. Phys.*, 1984, **57**, 59–246.

[27] H. Köppel, in *Conical intersections: electronic structure, dynamics and spectroscopy*, ed. W. Domcke, D. R. Yarkony and H. Köppel, World Scientific, New Jersey, 2004, ch. 10, pp. 429–472.

[28] I. B. Bersuker and V. Z. Polinger, *Vibronic Interactions in Molecules and Crystals*, Springer-Verlag, 1989.

[29] I. B. Bersuker, *The Jahn-Teller Effect*, Cambridge University Press, Cambridge, UK, 2006.

[30] C. A. Mead and D. G. Truhlar, *J. Chem. Phys.*, 1982, **77**, 6090–6091.

[31] H. Köppel, in *Conical intersections: electronic structure, dynamics and spectroscopy*, ed. W. Domcke, D. R. Yarkony and H. Köppel, World Scientific, New Jersey, 2004, ch. 4, pp. 175–204.

[32] R. J. Cave and J. F. Stanton, *J. Chem. Phys.*, 2014, **140**, 214112.

[33] R. J. Cave and J. F. Stanton, *J. Chem. Phys.*, 2016, **144**, 054110.

[34] K. Ruedenberg and G. J. Atchity, *J. Chem. Phys.*, 1993, **99**, 3799–3803.

[35] S. L. Li, D. G. Truhlar, M. W. Schmidt and M. S. Gordon, *J. Chem. Phys.*, 2015, **142**, 064106.

[36] H. Nakamura and D. G. Truhlar, *J. Chem. Phys.*, 2001, **115**, 10353–10372.

[37] H. Nakahara and D. G. Truhlar, *J. Chem. Phys.*, 2002, **117**, 5576–5593.

[38] H. K. Tran, J. F. Stanton and T. A. Miller, *J. Mol. Spectrosc.*, 2018, **343**, 102–115.

[39] A. Viel and W. Eisfeld, *J. Chem. Phys.*, 2004, **120**, 4603–4613.

[40] W. Eisfeld and A. Viel, *J. Chem. Phys.*, 2005, **122**, 204317.

[41] P. Mondal, D. Opalka, L. V. Poluyanov and W. Domcke, *Chem. Phys.*, 2011, **387**, 56–65.

[42] P. Mondal, D. Opalka, L. V. Poluyanov and W. Domcke, *J. Chem. Phys.*, 2012, **136**, 084308.

[43] S. Bhattacharyya, D. Opalka, L. V. Poluyanov and W. Domcke, *J. Phys. Conf. Series*, 2013, **428**, 012015.

[44] Z. Shao, H. Li, S. Zhang, J. Li, Z. Dai and Y. Mo, *J. Chem. Phys.*, 2012, **136**, 064308.

[45] D. Opalka and W. Domcke, *J. Chem. Phys.*, 2010, **132**, 154108.

[46] D. Opalka and W. Domcke, *Chem. Phys. Lett.*, 2010, **494**, 134–138.

[47] R. Sarkar, S. R. Reddy, S. Mahapatra and H. Köppel, *Chem. Phys.*, 2017, **482**, 39–51.

[48] T. Mondal, *Phys. Chem. Chem. Phys.*, 2018, **20**, 9401–9410.

[49] T. Zeng and I. Seidu, *Phys. Chem. Chem. Phys.*, 2017, **19**, 11098–11110.

[50] T. Zeng, R. J. Hickman, A. Kadri and I. Seidu, *J. Chem. Theory Comput.*, 2017, **13**, 5004–5018.

[51] R. A. Lang, A. Japahuge and T. Zeng, *Chem. Phys.*, 2018, **515**, 36–45.

[52] R. J. Hickman, R. A. Lang and T. Zeng, *Phys. Chem. Chem. Phys.*, 2018, **20**, 12312–12322.

[53] A. Viel, W. Eisfeld, S. Neumann, W. Domcke and U. Manthe, *J. Chem. Phys.*, 2006, **124**, 214306.

[54] A. D. Becke, *J. Chem. Phys.*, 1992, **96**, 2155–2160.

[55] C. Lee, W. Yang and R. G. Parr, *Phys. Rev. B*, 1988, **37**, 785–789.

[56] T. H. Dunning, *J. Chem. Phys.*, 1989, **90**, 1007–1023.

[57] M. W. Schmidt, K. K. Baldridge, J. A. Boatz, S. T. Elbert, M. S. Gordon, J. H. Jensen, S. Koseki, N. Matsunaga, K. A. Nguyen, S. Su, T. L. Windus, M. Dupuis and J. A. Montgomery Jr., *J. Comput. Chem.*, 1993, **14**, 1347–1363.

[58] M. S. Gordon and M. W. Schmidt, in *Advances in electronic structure theory: GAMESS a decade later*, ed. C. E. Dykstra, G. Frenking, K. S. Kim and G. E. Scuseria, Elsevier, Amsterdam, 2005, ch. 41, pp. 1167–1189.

[59] S. Bhattacharyya, Z. Dai and W. Domcke, *J. Chem. Phys.*, 2015, **143**, 194301.

[60] H. Nakano, R. Uchiyama and K. Hirao, *J. Comput. Chem.*, 2002, **23**, 1166–1175.

[61] M. Miyajima, Y. Watanabe and H. Nakano, *J. Chem. Phys.*, 2006, **124**, 044101.

[62] R. Ebisuzaki, Y. Watanabe and H. Nakano, *Chem. Phys. Lett.*, 2007, **442**, 164–169.

[63] T. Zeng, *J. Chem. Phys.*, 2017, **146**, 144103.

[64] C. M. Oana and A. I. Krylov, *J. Chem. Phys.*, 2007, **127**, 234106.

[65] H. D. Meyer, U. Manthe and L. S. Cederbaum, *Chem. Phys. Lett.*, 1990, **165**, 73–78.

[66] M. H. Beck, A. Jäckle, G. A. Worth and H.-D. Meyer, *Phys. Rep.*, 2000, **324**, 1–105.

[67] G. A. Worth, M. H. Beck, A. Jäckle and H.-D. Meyer, *The MCTDH Package, Version 8.2, (2000), University of Heidelberg, Heidelberg, Germany. H.-D. Meyer, Version 8.3 (2002), Version 8.4 (2007). O. Vendrell and H.-D. Meyer, Version 8.5 (2011).*

[68] C. A. Mead and D. G. Truhlar, *J. Chem. Phys.*, 1979, **70**, 2284–2298.

[69] M. V. Berry, *Proc. R. Soc. Lond. A*, 1984, **392**, 45–57.

[70] J. Schön and H. Köppel, *J. Chem. Phys.*, 1995, **103**, 9292–9303.

[71] J. Schön and H. Köppel, *J. Chem. Phys.*, 1998, **108**, 1503–1513.

[72] I. G. Ryabinkin, L. Joubert-Doriol and A. F. Izmaylov, *Acc. Chem. Res.*, 2017, **50**, 1785–1793.

[73] F. S. Ham, *Phys. Rev. Lett.*, 1987, **58**, 725–728.

[74] H. Koizumi and I. B. Bersuker, *Phys. Rev. Lett.*, 1999, **83**, 3009–3012.